Solvent-free extrusion of a LiFePO4-based monofilament for three-dimensional printing of a lithium-ion battery positive electrode

Victor Boudeville, Sylvie Grugeon, Alexis Maurel, Raynald Lesieur, Maroua Louati, Aurélie Cayla, Sébastian Ursescu, Christine Campagne, Stéphane Panier, Loic Dupont

Journal of Power Sources 593 (2024) 233973

Contents lists available at ScienceDirect

Journal of Power Sources

journal homepage: www.elsevier.com/locate/jpowsour

Solvent-free extrusion of a $LiFePO_4$-based monofilament for three-dimensional printing of a lithium-ion battery positive electrode

Victor Boudeville [a,b], Sylvie Grugeon [a,b], Alexis Maurel [a,b,c,e], Raynald Lesieur [a,b], Maroua Louati [d], Aurélie Cayla [d], Sébastian Ursescu [a,b], Christine Campagne [d], Stéphane Panier [a,e], Loic Dupont [a,b,f,*]

[a] Laboratoire de Réactivité et Chimie des Solides, CNRS UMR 7314, Université de Picardie Jules Verne, 15 rue Baudelocque, 80000, Amiens, France
[b] Réseau sur le Stockage Electrochimique de l'Energie, CNRS RS2E FR3459, France
[c] Department of Aerospace and Mechanical Engineering, The University of Texas at El Paso, El Paso, TX, 79968, USA
[d] Univ. Lille, ENSAIT, ULR 2461 - GEMTEX - Génie et Matériaux Textiles, F-59000, Lille, France
[e] Laboratoire des Technologies Innovantes, LTI-EA 3899, Université de Picardie Jules Verne, 80025, Amiens, France
[f] Plateforme de Microscopies Electronique de l'UPJV, 15 rue Baudelocque, 80000, Amiens, France

HIGHLIGHTS

- Successful implementation of FFF to 3D print high performance positive electrodes.
- Use of a thermoplastic elastomer to increase the filament flexibility.
- Prevailing impact of polymer rheology on fillers localization.
- Prediction of the ability of the filament to be rolled around a spool.

GRAPHICAL ABSTRACT

Left: Drawing illustrating the 3D printing of a battery. Right: Performance of a printed positive electrode with its microsctruture and roughness given in inset.

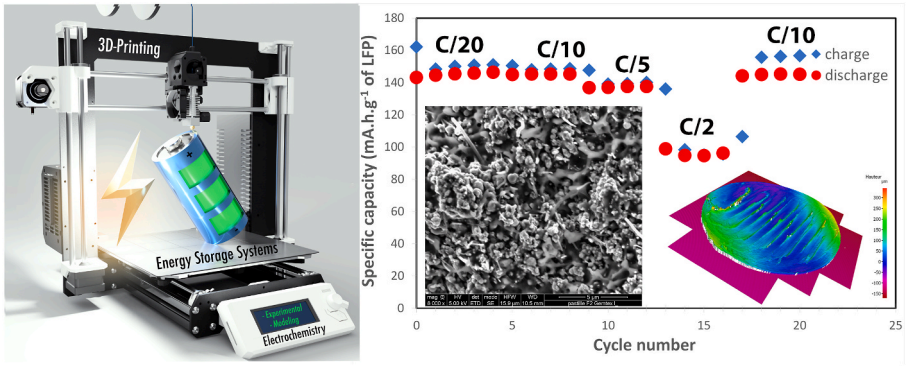

ARTICLE INFO

Keywords:
3D printing
Lithium ion battery
Polymer blend
Filled polymer
$LiFePO_4$
Solvent-free method

ABSTRACT

To meet the final objective of 3D printing a high-performance liquid-electrolyte lithium-ion battery using Fused Filament Fabrication (FFF), a positive electrode filament formulation based on $LiFePO_4$ and carbon nanofibers (CNF) is, herein, in-depth investigated. A highly-loaded composite monofilament containing a co-continuous structure of an immiscible non-polar (polypropylene-PP) and polar (polycaprolactone-PCL) thermoplastic polymers blend is successfully produced by hot-melt extrusion. This specific formulation confers desirable properties to the 3D printed electrode such as a mechanical integrity during cycling and good affinity with the electrolyte. Furthermore, for up-scale purpose, the incorporation of an optimal amount of thermoplastic

* Corresponding author. Laboratoire de Réactivité et Chimie des Solides, CNRS UMR 7314, Université de Picardie Jules Verne, 15 rue Baudelocque, 80000, Amiens, France.
E-mail address: loic.dupont@u-picardie.fr (L. Dupont).

https://doi.org/10.1016/j.jpowsour.2023.233973
Received 7 September 2023; Received in revised form 9 November 2023; Accepted 10 December 2023
Available online 22 December 2023

elastomers (TPE) into the filament composite to gain in flexibility is examined and its ability to be rolled around a spool at the extruder exit is modelled on the basis of experimental values of mechanical properties. In addition, it is shown that the larger-scale extruded filament has better electronic properties and the corresponding 3D-printed electrode exhibits excellent electrochemical behavior, making it possible to envisage an industrial scale-up production.

1. Introduction

Ever more innovative wearable technologies make our modern daily life simpler and enjoyable but in return requires more and more efficient energy storage devices, which pushes breakthrough developments. In 1991, an important turning point had been reached with the commercialization of the first Li-ion battery (LIB) by Sony Corporation [1,2]. LIB responded to all limitations of the older technologies, Ni/Cd and Ni-MH, i.e. higher energy storage, low self-discharge, fast charging, light weight and long cycle life [3]. Since then, the LIB storage capacity has quadrupled owing to major developments in chemistry but also through a better utilization of the battery components, reducing their inactive fraction. However, a leap towards higher performances is still deemed possible thanks to a cell re-design. Indeed, over the last decade, additive manufacturing (AM), known as 3D printing has provided a new opportunity to develop Li-ion batteries with a geometrically intricate structure [4] that could improve electrochemical performances. Indeed, a 3D architecture would increase the electrochemical active surface area and allow a two-dimensional or three-dimensional diffusion of the lithium ions, leading to higher rate capability [5]. Furthermore, printed in a single step and in any desirable geometry, these shape-conformable batteries could fit the final object housing such as smart glasses, smart watches, smart clothes, etc … [6–10] hence maximizing energy storage while reducing free volume.

Considerable effort has therefore been devoted to manufacturing Li-ion battery electrodes using additive manufacturing. Several teams have focused on the inkjet printing process most commonly named direct ink writing (DIW), which enables highly-charged electrodes to be printed with a high resolution of around 40-50 μm. Kohlmeyer et al. [11] printed a positive electrode ink made of polyvinylidene fluoride (PVDF), lithium iron phosphate ($LiFePO_4$ -LFP-) and carbon nanofibers (CNFs) (20/40/40 wt ratio) as dry materials and N-methyl-2-pyrrolidone (NMP) as solvent. The electrochemical performances tested with a commercial electrolyte composed of 1 M $LiPF_6$ in 1:1 ethylene carbonate:diethyl carbonate (EC:DEC) display a proper functionality of the printed electrodes; 156 $mAh.g^{-1}$ at C/5 and 106 $mAh.g^{-1}$ at 5C. Four years later, with the aim to elaborate a flexible battery, Bao et al. [12] used the same AM technique. The ink was also composed of the PVDF polymer and LFP materials. The difference lay in replacing CNFs with multiwall carbon nanotubes (MWCNTs), a more conductive carbon, and in using a different ratio with higher content of PVDF and lower content of carbon, PVDF/LFP/CNT (50/33/17 wt ratio). A similar discharge capacity of 154.5 $mAh.g^{-1}$ was reached at a slightly higher C-rate of C/3 with similar electrolyte. Gu et al. [13] showcased the good cycling capability (150 and 130 $mAh.g^{-1}$ at C/10 and 1C, respectively) of a highly-loaded LFP cathode (80 wt% of active material) prepared by inkjet printing of a sodium carboxymethyl cellulose (CMC)-based aqueous ink on a CNT paper collector. To go further, Khudiyev et al. [14] developed a Li-ion fiber battery using a judicious thermal drawing method. Thanks to very fine adjustment of viscosities and temperatures, three gels composed of cyclic carbonate electrolyte and PVDF for the separator, to which LFP or LTO and carbon black were added for the electrodes, were printed together with the collectors and casing to build a functional fiber battery in one-shot. Considering the above, DIW is considered a promising process for the manufacture of batteries, which however requires in-depth studies devoted to determining the impact of the size distribution of the particles and ink rheological properties on state of dispersion. In addition, post-treatment is imperative to remove the organic or aqueous solvent, thereby generating porosity and consolidating the electrode [15].

Other researchers laid the emphasis on printing batteries via fused filament fabrication (FFF). For instance, Ragones et al. [16] 3D printed LFP-based cathode from a filament composed of polylactic acid (PLA), LFP and conductive carbon in a 40/50/10 wt ratio. To ensure even dispersion of the materials in the filament, all materials fed into the extruder were pre-mixed using a solvent-based method. Despite this step, the cathode electrochemical performances were approximately 60, 50 and 20 $mAh.g^{-1}$, at 9, 44 and 88 $\mu A\ cm^{-2}$ which represents less than 50 % of the theoretical capacity of the LFP. It was suggested that this promising concept would require optimization of the composition and morphology of electrodes, compatibility and miscibility of components, and the parameters of the FFF printing technique to achieving full utilization of the active material using solvent-free process.

Pursuing on this work and our initial objective of manufacturing LIB cells by the use of FFF [17–19] 3D printing process, the present effort aims at improving the electrochemical performances of the positive electrode previously developed by Maurel et al. [20] for proof-of-concept purpose. In their work, the solvent tape casting process was also used to pre-mix all components, followed by the extrusion and the printing processes. The main limitation of the printed electrode composed of LFP and carbon black powders, PLA thermoplastic polymer and the plasticizer, polyethylene glycol dimethyl ether (PEGDME500) in a 49/5/33/13 wt ratio, relied on the PLA's affinity for carbonate-based liquid electrolyte. This property positively ensures a proper Li^+ ion conductivity within the electrode but also leads to a loss of its structural integrity upon cycling. In order to successfully reconcile the mechanical properties of the electrode with the expected long-term electrochemical performance, the envisioned strategy was to replace the single polymer PLA by a blend of two immiscible thermoplastic polymers with a co-continuous morphology [21–23], thus offering complementary functions; a non-polar olefin-type polymer endows the electrode with mechanical stability [25]. This polymer should contain the fillers (active material and carbon additives) to keep them well maintained and electronically connected after electrolyte soaking. The second polar polymer must have affinity for liquid electrolytes, hence promoting its uptake capability.

Thus, this research focuses on the manufacture, through solvent-free extrusion, of a highly loaded positive electrode filament composed of LFP, carbon and the two non-polar and polar polymers, polypropylene (PP) and polycaprolactone (PCL), with proper fillers localization and mechanical properties adapted to FFF implementation. However, from a mechanical point of view, as incorporating a large quantity of fillers leads to the brittleness of the polymer blend, the addition of a third thermoplastic elastomer-type polymer is in-depth investigated in order to give the filament enough flexibility to be rolled around a spool when processed at industrial scale. After predicting the fillers localization through wettability coefficient determination and viscosity measurements [26], spoolability of filaments as function of elastomer content is modelled from tensile test data and verified experimentally. Afterwards, the impact of the elastomer on 3D printed discs electrochemical performances is discussed based on filaments electronic conductivity measurement and microscopy, porosity and accessibility analysis. Finally, the electrochemical properties of electrodes 3D printed from the best-performing monofilament obtained by larger-scale extrusion are compared.

2. Experimental/methods

Materials for extrusion: The polypropylene (PP) pellets were kindly provided by Nanovia company and polycaprolactone pellets (PCL, Capa 6400) were purchased from Perstorp Holding AB. The polypropylene (85 wt%) – *block* - polyethylene (15 wt%)-based elastomer pellets (PBE, 38.7 kg/mol, Vistamaxx™ Performance Polymer 6202) were provided by ExxonMobil. The positive active material $LiFePO_4$ (LFP, pulverized morphology type, particle size D50: 2-6 μm, 11-15 $m^2\ g^{-1}$, carbon content: 1.3–1.6 %) was kindly provided by the company Aleees, Taiwan. Carbon nanofibers (CNF, 24 $m^2\ g^{-1}$, fibers (100 nm x 20–200 μm) and nodules (<1 μm) entangled in 50 μm diameter balls) were purchased from Sigma-Aldrich.)

Laboratory-scale filament extrusion: The filaments were produced by means of the micro compounder (total volume of 7 cm^3), Haake Minilab 3, Thermofischer SCIENTIFIC equipped with conical co-rotative twin screws, an integrated bypass valve enabling the recirculation of the melt via a backflow channel for a better mixing of the polymer composite materials, and a 2 mm diameter nozzle. The manual introduction of the components into the extruder was carried out in two stages (Fig. 1). Polymers were introduced first in recirculation mode, to ensure homogeneity of the melt mixture, and after 10 min, the intimate blend of the fillers, LFP and CNF, was added. These two powders were previously mixed for 10 h in a container containing zircon beads, by using a Turbula® shaker mixer. The extrusions were all performed at a temperature of 215 °C. The screw speed was maintained at 50 rpm throughout the extrusion process. This rotation speed was estimated to correspond to a shear strain rate of 4 s^{-1} according to some rheological experiments carried out thanks to the two pressure sensors placed in the recirculation channel. The residence time after all loads have been introduced in the micro compounder was set at 10 min. At the exit of the extruder, the filament was cooled during its stay on the conveyor belt under atmospheric conditions, then, was stored at 45 °C to avoid moisture absorption.

Large-scale filament extrusion: Filaments were produced using the Process 11 twin-screw parallel extruder, Thermofischer SCIENTIFIC. The screw ratio, length (44 cm)/diameter (11 mm), was 40. The screws consisted of a sequence of different elements: feeding then alternately, mixing and discharge elements. The materials were introduced into the extruder at a temperature of 215 °C and a screw rotation speed of 100 rpm, following the sequence: All polymers are extruded together. The resulting filament is then pelletized. Afterwards, the pellets are mixed with the LFP and CNF powders previously mixed in the same way as for the laboratory-scale extrusion. The blend of polymers, LFP and CNF is introduced (around 50 g) in the extruder and the 1.75 mm diameter filament is collected around a spool.

Mechanical characterization of filaments: Tensile tests on filaments obtained from extrusion were carried out with a Criterion 10 kN testing machine from MTS. Filaments diameter has been measured before every tensile test. The filament was fixed between two clamps separated by a distance of 100 mm. Tests were controlled by displacement with a speed of 100 mm min^{-1}. For each filament composition, five specimens have been tested.

Printing: 3D printing of the filaments in the form of 10 mm diameter and 0.2 mm thick discs was carried out using the Original Prusa i3 MK3 3D printer. The disc was designed using Autodesk® Fusion 360 software and sliced to print specifications using PrusaSlicer 2.5.0 software. The outlet nozzle diameter was 0.6 mm, to allow printing of highly-loaded filament. Printing parameters such as print speed and nozzle and bed temperatures were tuned to 20 mm s^{-1}, 220 °C and 50 °C, respectively.

Wettability coefficient. The wettability coefficient of LFP in the blend of immiscible polymers was calculated according to the equations of Fowkes et al. [25] and Caridnaud et al. [2] This calculation requires the experimental determination of the surface energy values through contact angle measurements, this value being equal to the sum of its polar and dispersive components. The latter were obtained from the GBX MCAT V6 Digidrop machine using the Sessile method [26]. 20 measurements of contact angles were performed with polar (distilled water) and non-polar (diiodomethane or α-bromonaphtalene) liquids. The neat polymer pellets (PP, PBE and PCL) were previously thermocompressed as follows: the pellets were placed between heated PTFE plates for 5 min without pressure, then a pressure of 70 bar was applied at 10 °C above the melting temperature (thus corresponding to 180 °C, 110 °C [27] and 70 °C, respectively). The plates, still under pressure, were then cooled to room temperature to form an approximately 1 mm thick moulded plate on the surface of which the drop of liquid was deposited. As for charges, an LFP pellet was made by a flash sintering process. Unfortunately, it was not possible to make a CNF pellet.

Viscosity analysis: The viscosity of the polymers was measured using a Malvern KINEXUS plane/plane rheometer. The gap between planes was 1 mm and the shear strains were recorded in the range of 1–60 s^{-1}. The temperature was set at the maximum temperature of 200 °C to ensure complete melting of the polymer.

Electronic conductivity of filaments: The procedure was inspired by the

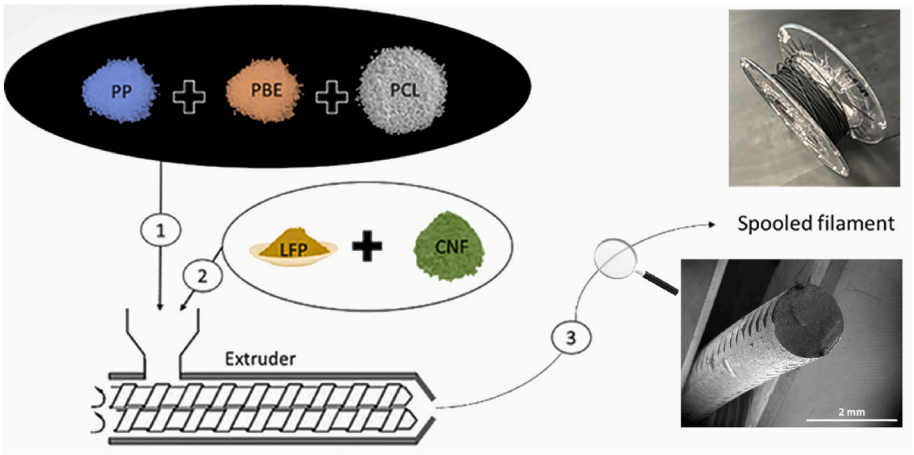

Fig. 1. Extruder feeding steps. Note that the PBE is introduced at the same time as PP and PCL. SEM image of the filament and image of the spooled filament are added in insets.

one described by Multi3D LLC. The resistance measurements on filaments were carried out using a multimeter (RS PRO HS-608) by placing 2 clamps at different lengths, 2.5, 5 and 10 cm. The following equation was used to calculate the conductivity (σ) $\sigma = \frac{1}{R} \times \frac{L}{A}$ where R is the measured resistance of the filament (Ω), L is the length of the filament, and A is the cross-sectional area (cm^2). A caliper was used to measure the diameter of the filament. Three measurements were made for the 3 different lengths to check repeatability.

Scanning and transmission electron microscopy: The 3D printed disks cross-section, top and bottom were studied by scanning electron microscopy (SEM) to verify the polymers structural morphology and charges localization. To gain access to the cross-section of the printed disks, the samples were frozen in liquid nitrogen and broken in half with the assistance of tweezers. The instrument used was the FEI Quanta 200F (Thermo Fisher Scientific) and the images were acquired in high-vacuum mode with an acceleration voltage of 5 kV for both secondary and backscattered electrons modes. The charges dispersion within the polymers matrix was examined via transmission electron microscopy (TEM) by means of a FEI Tecnai F20 ST electron microscope operating at 200 kV. Beforehand, filament was cut and inserted in a capsule in which a LR white resin (Sigma-Aldrich) was added drop by drop. The resulting capsule was then placed in an oven at 70 °C during 24h. A microtome (RMC Products, Boeckeler) was then used to cut the capsules in thin slices (sections) of material of 100 nm at a cutting speed of 21.5 mm s^{-1}. Slices were finally deposited onto a holey carbon copper grid for the PLA-based sample and on a nickel grid for the PP/PCL sample.

Polymer selective extraction: As PCL is intended to promote electrolyte uptake throughout the 3D printed disc, its selective dissolution was undertaken to measure its accessibility. The electrode discs were soaked in dichloromethane for 24 h at room temperature. The percentage accessibility was calculated after measuring the mass loss of the discs after the PCL dissolution and drying, following equation (1) [22].

$$Accessibility\ (\%) = \frac{(m\ (3D\ printed\ disc\ before\ soaking) - m\ (3D\ printed\ disc\ after\ soaking)}{m\ (3D\ printed\ disc\ before\ soaking) * wt\ (percentage\ PCL\ massic\ ratio)} * 100 \quad \text{(Equation 1)}$$

Helium picnometry (porosity measurements): A Micromeritics Accupyc 1330 equipment was used for He picnometry. Measurements were carried out on five 3D printed discs. The electrode volume porosity (p) is estimated considering the difference between the geometric volume (sample thickness x sample geometric area) and the measured volume.

Electrochemical measurement: Coin cells were assembled in an argon-filled glovebox (H_2O < 0.1 ppm, O_2 < 0.1 ppm). 3D printed discs were used as working electrode and metallic lithium as reference and counter electrode. A glass fiber separator supplied by Whatman, GE Healthcare was filled with 150 μL of the electrolyte composed of 1 M $LiPF_6$ in ethylene carbonate and dimethyl carbonate (EC/DMC, 3:7 wt ratio). After assembling, cells were subjected to a resting time of 12 h then a cycling protocol in galvanostatic mode at 25 °C, at the following rates; a charge at C/40, a discharge at C/20, then four cycles at C/20, C/10, C/5, C/2 then C/10, in the voltage range of 2.8–4 V (*vs.* Li/Li^+). All cells were cycled using the galvanostat BCS-805 (BioLogic, France).

3. RESULTS and DISCUSSION

3.1. Investigated positive electrode composite filament formulations

Achieving dual ionic and electronic percolation within the highly filled 3D printed positive electrode was the challenge to overcome in order to have good electrochemical performances. To this end, a composite with a co-continuous morphology of the two immiscible polymers previously studied by our team [24], PP and PCL, was considered, as well as a selective placement of fillers (active material and conductive carbon) in the non-polar PP polymer matrix. PP is a semi-rigid polymer used in the composition of the classic separators of today's lithium-ion batteries. It has high mechanical stability even when in contact with electrolyte solutions. On the contrary, PCL is a polar polymer featuring a high affinity with electrolytes, thus facilitating the transport of ions into the electrode. Thus, if well-held in the PP matrix, fillers should form a sustainable electronic network while the liquid carbonate-based electrolyte could reach the active material particles after the formation of a gel with PCL. As an alternative to the addition of more or less volatile plasticizers to make the filament more flexible, PP (23.7 wt%) was substituted by different proportions of the thermoplastic elastomer PBE (filaments with 0, 25, 50 and 100 % of PBE are called F1, F2, F3 and F4, respectively, Table 1) while the amount of LFP, CNF and PCL was kept constant (55.5/5.5/15.8 wt ratio, the (PP + PBE)/PCL wt. polymer ratio was equal to 60/40).

PP-b-PE-based elastomers which have a high flexibility, are easy to process and have little impact on the thermal properties of PP. Indeed, from DSC measurements carried out at a rate of 10 °C/min, PP in F1, F2 and F3 printed discs displays crystallinity respectively of 56, 52 and 50 % with a melting temperature of around 151 °C, 154 °C and 153 °C and a crystallization temperature of around 126, 127 and 124 °C. From literature, using PBE, PP's flexibility might be significantly enhanced while maintaining other appropriate properties until 30 wt% content of PBE [28]. Blending PBE with PP can also improve impact resistance, and improve its processing properties [29]. According to Global Source website, the ratio between the price per kg of PBE on PP one is about 1.8. Unfortunately, substituting 25 % by weight of PP with PBE would increase the cost of non-polar polymers (PP + PBE) by approximately 20 %.

3.2. Prediction of loads localization in immiscible polymers

To help predict the preferential distribution of fillers in one or the other of the two polymers (PCL/PP or PCL/PBE), wetting coefficient and polymer viscosities were beforehand investigated.

The wetting coefficient is defined as a ratio of the interfacial energies between the filler and the polymers and between both polymers (Eq. (2)):

$$\omega_{pol\ A-pol\ B} = \frac{\gamma_{filler-pol\ B} - \gamma_{filler-pol\ A}}{\gamma_{pol\ A-pol\ B}} \quad \text{(Equation 2)}$$

Where $\gamma_{filler\text{-}pol\ B}$, $\gamma_{filler\text{-}pol\ A}$ and $\gamma_{pol\ A\text{-}pol\ B}$ are interfacial energies, respectively, between fillers and polymer B, between fillers and polymer A, and between polymer A and polymer B. Moreover, to determine the filler localization, the following conditions need to be considered [30].

- If $\omega_{pol\ A-pol\ B} < -1$, fillers will be localized in only polymer B.
- If $1 > \omega_{pol\ A-pol\ B} > -1$, fillers will be selectively localized at the interface of the two polymers.
- If $\omega_{pol\ A-pol\ B} > 1$, fillers will be localized only in polymer A.

The interfacial energy between two constituents 1 and 2 can be calculated (Eqs. 3 and 4) according to Ref. [31].

Table 1
Formulation of the positive electrode filaments with increasing amount of PBE (PP/PBE wt. ratio of 100/0, 75/25, 50/50, and 0/100 corresponding to formulations F1, F2, F3 and F4, respectively). For weight-volume conversion, materials densities were determined by helium pycnometry ($d_{PP} = 0.90$, $d_{PBE} = 0.9$, $d_{PCL} = 1.15$, $d_{LFP} = 3.51$, $d_{CNF} = 1.9$).

	PP		PBE		PCL		LFP		CNF	
	wt%	vol%	wt%	vol%	wt%	vol%	wt%	vol%	wt%	vol%
F1	23.7	*44.9*			15.8	*23.4*	55	*26.7*	5.5	*4.9*
F2	17.8	*33.7*	5.9	*11.2*						
F3	11.8	*22.5*	11.8	*22.5*						
F4			23.7	*44.9*						

Table 2
Contact angle measurements with polar and non-polar liquids.

	Polar liquid	Non-polar liquid
PP	86.9° ± 4.4°	32.7° ± 7.2°
PCL	69.6° ± 3.9°	36.4° ± 3.5°
PBE	90.8° ± 3.8°	50.7° ± 5.5°
LFP	71.8° ± 6.5°	65.5° ± 6.0°

- the harmonic-mean: $\gamma_{1-2} = \gamma_1 + \gamma_2 - \frac{4\gamma_1^d\gamma_2^d}{\gamma_1^d+\gamma_2^d} - \frac{4\gamma_1^p\gamma_2^p}{\gamma_1^p+\gamma_2^p}$ (Equation 3)
- the geometric-mean: $\gamma_{1-2} = \gamma_1 + \gamma_2 - 2\sqrt{\gamma_1^d\gamma_2^d} - 2\sqrt{\gamma_1^p\gamma_2^p}$ (Equation 4)

where γ_i is the surface energy of constituent i; γ_i^d and γ_i^p are, respectively, its dispersive and polar component.

Polar and dispersive components of the surface energies were obtained from contact angle measurements for the polymers PP and PCL, the elastomer PBE and the LFP powder. The average and standard deviation of the measured angles are given in the Table 2.

In Table 1, we can remark a high variability in contact angle measurements. There are several sources of variability as the imperfections of the surface, the technique used to place the drop of liquid on the surface (there is not one contact angle for a given liquid/solid pair, but rather a range of stable contact angles), the goniometer precision … Due to this variability, a Monte Carlo method was used to evaluate the surface energy, interfacial energy and wetting coefficient which are considered as the outputs. From average and standard deviation of the Table 2, standard normal distributions of the different contact angles were defined and used as input for the Monte Carlo's approach. 10^5 simulations were done to evaluate the different outputs. The surface energy, interfacial energy and wetting coefficient obtained with the Monte Carlo simulations are given in Tables 3–5 considering the 2 types of mean for the interfacial energy evaluation.

From Table 4, we can remark that for all the couples of materials, the predicted interfacial energy with geometric-mean is lower than the value obtained with harmonic mean. This trend was previously observed in other studies [24]. The obtained interfacial energy between PP and

Table 3
Calculated surface energy and its components (dispersive and polar).

	Surface energy (mN/m)	Dispersive component (mJ/m^2)	Polar component (mJ/m^2)
PP	39.6 ± 2.6	37.6 ± 2.7	2.0 ± 1.2
PCL	45.1 ± 2.1	36.4 ± 1.4	8.7 ± 1.9
PBE	32.0 ± 2.4	29.7 ± 2.7	2.3 ± 1.1
LFP	34.1 ± 4.0	18.8 ± 3.6	15.3 ± 5.3

Table 4
Interfacial energy between PP, PCL, PBE and LFP fillers.

	Interfacial energy (mJ/m^2) (harmonic mean)	Interfacial energy (mJ/m^2) (geometric mean)
γ_{LFP-PP}	17.5 ± 2.6	10.4 ± 5.5
$\gamma_{LFP-PCL}$	8.8 ± 5.1	4.6 ± 2.8
$\gamma_{LFP-PBE}$	13.0 ± 6.9	7.8 ± 4.6
γ_{PP-PCL}	4.7 ± 2.4	2.8 ± 1.7
$\gamma_{PBE-PCL}$	4.9 ± 2.1	2.8 ± 1.4

Table 5
Wetting coefficient values and predicted LFP filler localization.

	Wetting coefficient (harmonic mean)	Wetting coefficient (geometric mean)	Prediction of the LFP particles localization
ω_{PP-PCL}	−2.1 ± 1.9	−2.5 ± 2.2	In PCL with 70 % of confidence level
$\omega_{PBE-PCL}$	−0.8 ± 0.9	−1.1 ± 1.0	In PCL with 41 % and 55 % of confidence level respectively for harmonic mean and geometric mean

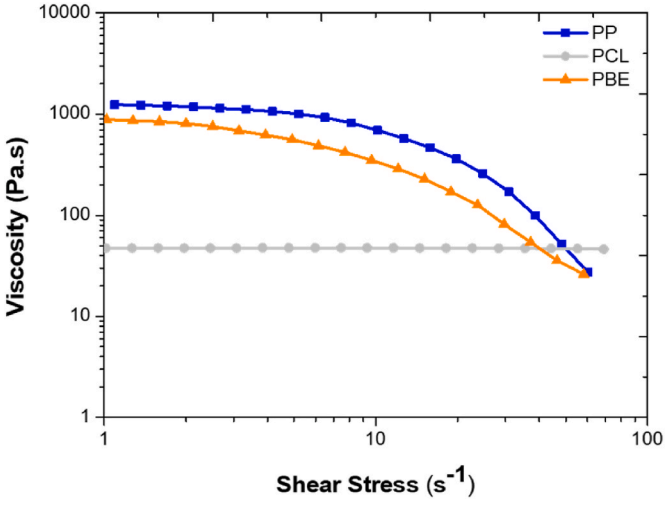

Fig. 2. Evolution of the viscosity of PP, PBE and PCL, measured at 200 °C, as function of shear strain rate over the [1-60 s^{-1}] range.

PCL is the same as the interfacial energy between PBE and PCL. The difference in the localization of the filler will then depend only on the numerator of the wetting coefficient.

Using Monte Carlo analysis, a confidence interval was determined for the location of LFP particles in the two polymer blends, PP/PCL and PBE/PCL (Table 5). Based on these calculations, in the PP/PCL blend, the LFP particles would be localized in PCL polymer with 70 % of confidence and in the PBE/PCL blend, LFP particles would be likely to be found in the PCL or at the interface between the PBE and the PCL. It is worth noting that these results are clearly the opposite of our expectations.

However, following the work of Plattier et al. [32], the localization of the particles is also driven by the viscosities of the polymers. Further studies on rheological properties of the neat polymers have thus been undertaken at 200 °C. It is noteworthy that this temperature, which corresponds to the maximum temperature of the rheometer, is lower than the extrusion and printing temperatures of 215 and 220 °C, respectively. Far above its melting point, the PCL polymer displays a Newtonian behavior with a constant viscosity value of 51 Pa s at 200 °C (Fig. 2). As for PP and PBE, they exhibit shear thinning behaviors. The viscosity of the molten PP and PBE decreases resp. from 1243 to 27 and 885 to 30 Pa s as the shear strain rate increases from 1 to 60 s^{-1}. According to Plattier et al. [32], fillers should be located in the most viscous polymer. Thus, it is safe to assume, from the viscosity values obtained at lower shear rates than 10 s^{-1} (the extrusion process at 50 rpm corresponding to a shear strain rate of 6 s^{-1}), that the fillers are more likely to be found in PP and PBE, both of which having a much higher viscosity value than PCL. In summary, the two approaches based on wettability coefficients or viscosities, do not lead to the same conclusion about the location of LFP in polymers. Relying on the results of the viscosity approach, the manufacture of the electrode filaments by extrusion was undertaken in the hope that the LFP particles would be found in the PP (or PBE). Note that, whatever the location of the CNF, these fibers are assumed to be long enough to pass through the large volume of polymers (total volume of 68.4 %) and create a conductive network that would percolate up to the LFP particles.

3.3. Laboratory-scale filament extrusion

The solvent-free extrusion process shown in Fig. 1 was implemented to produce the filaments F1, F2, F3 and F4 (Table 1). As the reference filament (F1) containing PP (23.7 wt%) only was too brittle to be wound up, the latter has been substituted by 25, 50 and 100 wt% of PBE. As expected, an increase in flexibility was observed with filaments containing an increasing amount of PBE. All filaments F2, F3 and F4 were successfully rolled around a spool at the exit of the micro compounder. To rationalize their spooling capability as a function of elastomer content, modelling based on experimental values of mechanical properties is used.

3.3.1. Mechanical characterization of filaments and spoolability modeling

Tensile tests were carried out to determine the mechanical properties of the filaments, namely, the elastic modulus E, the tensile strength and the elongation at break. For each formulation, these properties are given in Table 6. Theoretically, a filament is spoolable if its tensile strength is higher than the maximum stress reached during the spooling process. During the spooling process, a tension load N and bending moment Mb are applied on the filament. The tension load is generally neglected compared to the bending moment. The maximum stress σ_{max} can be evaluated considering the filament as an elastic material under pure bending (the curvature of the filament is circular). According to these assumptions, the bending moment is $M_b = EI/R$ and the maximum stress is given by the following equation (Eq. 5):

$$\sigma_{max} = \frac{M_b}{I}\cdot\frac{d}{2} = \frac{E.d}{2.R} \qquad \text{(Equation 5)}$$

Where E is the elastic modulus of the filament in MPa, R, the radius of the curvature of the filament in mm, I, the moment of inertia of the section of the filament in mm^4 and d is the diameter of the filament in mm. The minimum value of R is the radius of the spool around which the filament is wound up (R = 50 mm).

As anticipated, the elastic modulus of the filament decreases as the PBE content increases. F2 and F3 filaments behave as soft polymers while the F4 filament exhibits an elastomeric behavior with a much lower elastic modulus and higher elongation at break.

Fig. 3 compares the tensile strength (red dots) with the above-defined maximum stress (black square) of the four filaments. A filament is spoolable if the maximum stress σ_{max} during spooling is lower than the tensile strength i.e. the value is in the green zone of the Fig. 3. The σ_{max} for the F1 filament is in the red zone thus the filament is not spoolable. Its brittle behavior prevents it from twisting and, as a result, it breaks under high angular stress. On the contrary, the σ_{max} values corresponding to the F2, F3 and F4 filaments are situated in the green zone, thus filaments are spoolable. These theoretical conclusions on the spoolable character of filaments F2, F3 and F4 are in perfect agreement with the experimental observation made at the exit of the extruder.

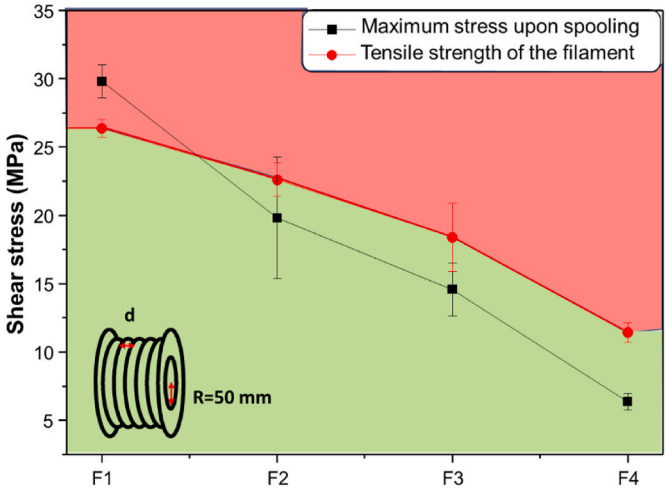

Fig. 3. Red dots correspond to the experimentally obtained tensile strength values. Black squares correspond to the maximum stress values calculated (Eq. (5)) for the filaments when rolled around a 50 mm radius spool (R). The maximum stress must be lower than the tensile strength to be spoolable, thus located inside the green region. (For interpretation of the references to colour in this figure legend, the reader is referred to the Web version of this article.)

Table 6
Tensile test results obtained on filaments F1, F2, F3 and F4. The maximum stress upon spooling is calculated according to equation (5).

	Elastic modulus (MPa)	Tensile strength (MPa)	Elongation at break (%)	Max. stress (σ_{max}) upon spooling (MPa)
F1	1958 ± 52	26.4 ± 0.6	2.0 ± 0.3	29.8 ± 1.2
F2	1418 ± 346	22.6 ± 1.2	3.0 ± 0.2	19.8 ± 4.4
F3	1043 ± 61	18.4 ± 2.5	2.8 ± 0.5	14.6 ± 1.9
F4	397 ± 56	11.4 ± 0.7	12.3 ± 1.6	6.4 ± 0.6

3.3.2. Electrochemical performance study

After demonstrating the PBE-based filaments F2, F3 and F4 were flexible enough to be rolled around a spool, they were used as feedstock to 3D printed positive electrode discs so as to assess their

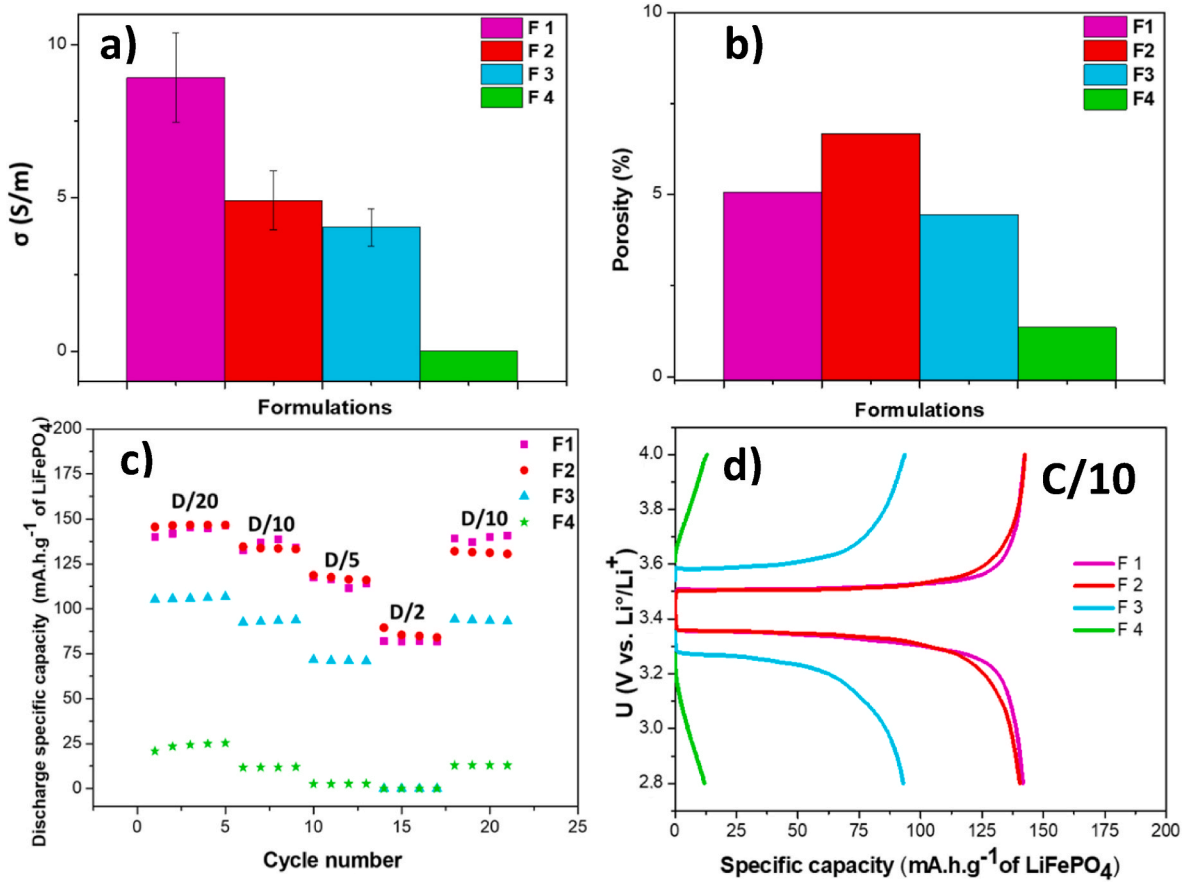

Fig. 4. a) Electronic conductivity of filaments, b) porosity of 3D printed discs and c) specific discharge capacity of discs printed with F1, F2, F3 and F4 filaments with increasing PBE/PP ratio. These cells have undergone the same C-rates of C/40, D/20 then C/n = D/n, n = 10, 5, 2 and 10 (D stands for C-rate upon discharge). d) Corresponding polarization curves obtained upon cycling at C/10.

electrochemical performance and determine the best formulation. Beforehand, the electronic conductivity of the filaments, the accessibility to PCL polymer and the porosity of printed discs were measured to assess the capability of the composite to conduct electrons and soak the electrolyte.

3.3.2.1. Electronic conductivity of composite filament. The four formulations have been investigated to get insight into the impact of PBE on the filament conductivity, all containing the same amount and type of carbon (Table 1). As shown in Fig. 4a, the conductivity decreases as the content of PBE increases. Values of 8.9 ± 1.5, 4.91 ± 0.96, 4.04 ± 0.61 and $4.10^{-3} \pm 2.10^{-3}$ S/m were obtained for F1, F2, F3 and F4, respectively. Surprisingly, the complete replacement of PP by PBE reduces electronic conductivity to a very low value. Two possible reasons could account for the decrease in conductivity; CNF particles are isolated from each other, maybe owing to a very covering insulating layer of polymer or fibers are not evenly dispersed within the composite due to poor disentanglement during extrusion. Overall, it can be anticipated from these results that formulations containing as little PBE as possible will be preferable when considering electrochemistry.

3.3.2.2. PCL accessibility and porosity measurements on 3D printed discs. Electrochemical study was performed on 10 mm diameter and 200 μm thickness electrode discs printed from filaments F1 to F4, according to the protocol described in experimental section. Prior to cycling, PCL selective dissolution tests were performed on these 3D printed discs to assess its accessibility in the blend. The mass difference measurements demonstrated that PCL was completely dissolved, irrespective to the filament formulation. It was then assumed that PCL would form a continuous network to allow the electrolyte to penetrate the composite through gelation and create an ionic path. It is worth mentioning that no residual solid particles were observed in the solution at the end of the dissolution time. This observation is in line with the above reported filler location prediction study based on viscosity, from which conclusion was drawn that LFP should be located in the mechanically stable olefin-type polymers, PP and/or PBE.

Further to these PCL accessibility measurements, porosity of the discs was measured by helium pycnometry (Fig. 4b). The pure PP-based disc corresponding to the F1 formulation exhibits porosity value around 5.07 ± 0.04 %. It remains almost the same value with F2 formulation, then, the porosity decreases slightly, to 4.45 ± 0.05 % and 1.36 ± 0.01 % respectively for F3 and F4. A high porosity should allow faster absorption of the liquid electrolyte within the disc. Such characteristic is of particular interest when considering the electrolyte filling of full 3D printed cells, a concern that was raised by Maurel et al. [20] while printing PLA-based full-cell components. In this respect, formulations containing low quantities of PBE should be preferred.

It is worth mentioning that PCL, in the F2 filament containing the lowest PBE quantity, represents a volume of 23.4 %. If we consider it as a component of the electrolyte after gelation, this volume can be considered as porosity, giving a total electrode porosity of about 30 % (23.4 (PCL) + 6.6 (by He pycnometer) = 30). This value is close to that of the current Li-ion battery electrodes. Furthermore, if we do not take the PCL into account when calculating the mass ratio of the LFP active material,

we obtain a value of 65.3 wt% (PP/PBE/LFP/CNF: 21.1/7.0/65.3/6.5 wt% and 44.1/14.6/34.9/6.4 vol%).

3.3.2.3. Cycling tests on 3D printed discs. After highlighting the harmful impact of high amount of PBE on the electronic conductivity and porosity of composites, an in-depth study was carried out to determine its electrochemical impact in half coin cell configuration. Fig. 4c portrays the evolution of the specific discharge capacity of the 3D printed discs for all formulations, F1 to F4.

The PBE-free disc of F1 formulation exhibits unprecedent specific capacities of around 145, 138, 116, 82 and 137 mAh per gram of LFP active material, at current rates of C/20, C/10, C/5, C/2 and C/10, respectively, the lower rate (C/20) capacity corresponding to around 85 % of the LFP theoretical capacity (170 $mAh.g^{-1}$). The specific discharge capacities are decreasing with C-rates. In addition to the high thickness of the electrodes (around 150–200 μm), two phenomena are assumed to cause a loss of ionic conductivity and thus affect the high-rate capability. i) The gelation of the liquid electrolyte in contact with the PCL, which increases the viscosity of the electrolyte and therefore decreases the ionic conductivity. In PCL/electrolyte paths, the diffusion of lithium ions within the gel is therefore slower than in a liquid, leading to a reduction in performance, especially at high C-rates. ii) The high amount of PP polymer, which represents 23.7 wt%/44.9 vol% (Table 1). This leads to an increase in tortuosity which also impedes the transport of lithium ions inside the electrode. It is noteworthy that similar capacities of around 140 $mAh.g^{-1}$ are observed while coming back at C/10 after cycling with successive increasing C-rate conditions. This suggests a good mechanical stability of the electrode upon cycling.

For more flexibility, the PP polymer was substituted by the elastomer PBE. Interestingly, the capacities of F2 discs are fairly similar to those of F1 disks for all studied C-rates. Then, F3 and F4 electrode discs witness a gradual decrease in capacity with increasing PBE/PP ratio; a capacity of around 106 $mAh.g^{-1}$ at the low current rate of C/20 was obtained for F3 disc, while the specific capacity of F4 discs abruptly drops to a very low value of 25 $mAh.g^{-1}$. The capacity loss is accompanied by a significant increase in polarization ($\Delta V = 0.17$ V, 0.2 V and 0.31 V for F1, F2 and F3, respectively at 60 $mAh.g^{-1}$) (Fig. 4d). PBE-containing filaments depict lower electronic conductivities (Fig. 4a), which can explain this result. It seems clear that a large amount of PBE prevents certain particles of active material from being electronically (and perhaps ionically) accessible and participating in electrochemical reactions.

3.3.3. Morphological study of the cross-section of 3D printed discs using SEM analysis

To get further information regarding the localization and dispersion of the materials and shed light on the impact of PBE on electrochemical performances, the morphology of 3D printed discs cross-sections was studied using SEM. F1 disc (Fig. 5a) clearly reveals polymeric domains that do not contain LFP particles; only CNF fibers have been seen, crossing them. As these polymer domains tend to melt easily under the electron beam, we can assume that they correspond to the PCL matrix. It should be noted that the hereabove described viscosity study predicted the preferential location of LFP in PP. The SEM observations show that, in this case, this approach prevails over that based on the wettability coefficient, the latter having predicted LFP in PCL. Furthermore, F1 and F4 discs depict different structures. In F1 sample (Fig. 5 a and b), the CNF fibers look partially detached from the polymer matrix and present a clean surface. It can be remarked an orientation of fibers (Fig. 5a), they are aligned with the direction in which the printhead deposits material. In the PBE-containing F4 sample (Fig. 5c), fibers appear to be covered by a polymer. As a result, they struggle to come into contact with each other, which explain the gradual decline in electronic conductivity and electrochemical performance as a function of the PBE content.

Considering all the above, F2 filaments, with the lower amount of PBE, seem to represent the best compromise between mechanical properties, i.e. the ability to be rolled around a spool, and electrochemical performances. This formulation was thus chosen to experience larger-scale manufacture.

3.4. Comparison with previous study on single polar polymer composite

The above outcomes obtained for F2 formulation are worth comparing with that obtained in our previous study [20]. The work from A. Maurel et al. focused on 3D printed LFP electrode discs formulated with a single PLA polar polymer and carbon black (33/13/49/5 wt ratio for PLA/plasticizer (PEGDME500)/LFP/carbon black). Those discs of around the same 150-200 μm thickness and composed of same carbon-coated LFP material display a much lower capacity of around 90 $mAh.g^{-1}$ at C/20 (compared to 148 $mAh.g^{-1}$ for F2), which corresponds to only 53 % of the LFP theoretical capacity. In this regard,

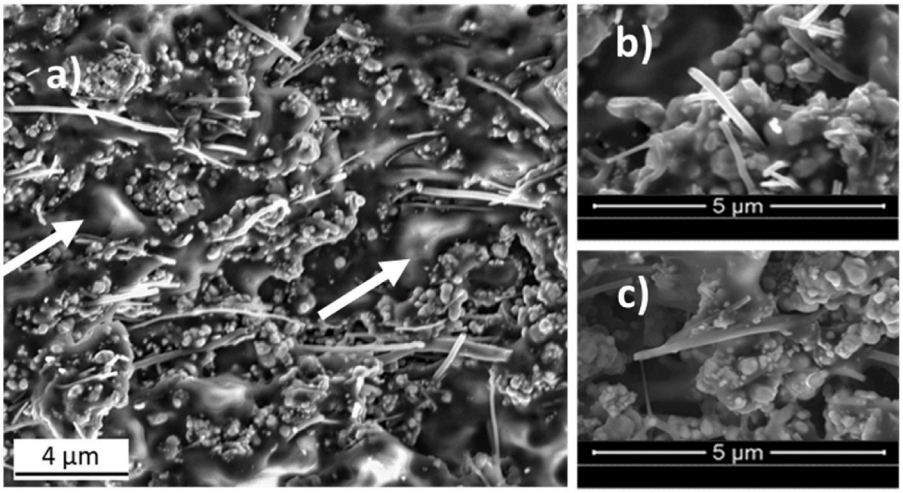

Fig. 5. Cross-section SEM images of 3D printed discs with a, b) F1 and c) F4 filaments. Two arrows in a) show PCL domains without LFP particles. b) shows a carbon nanofiber with a clean surface c) shows a carbon nanofiber coated by PBE polymer.

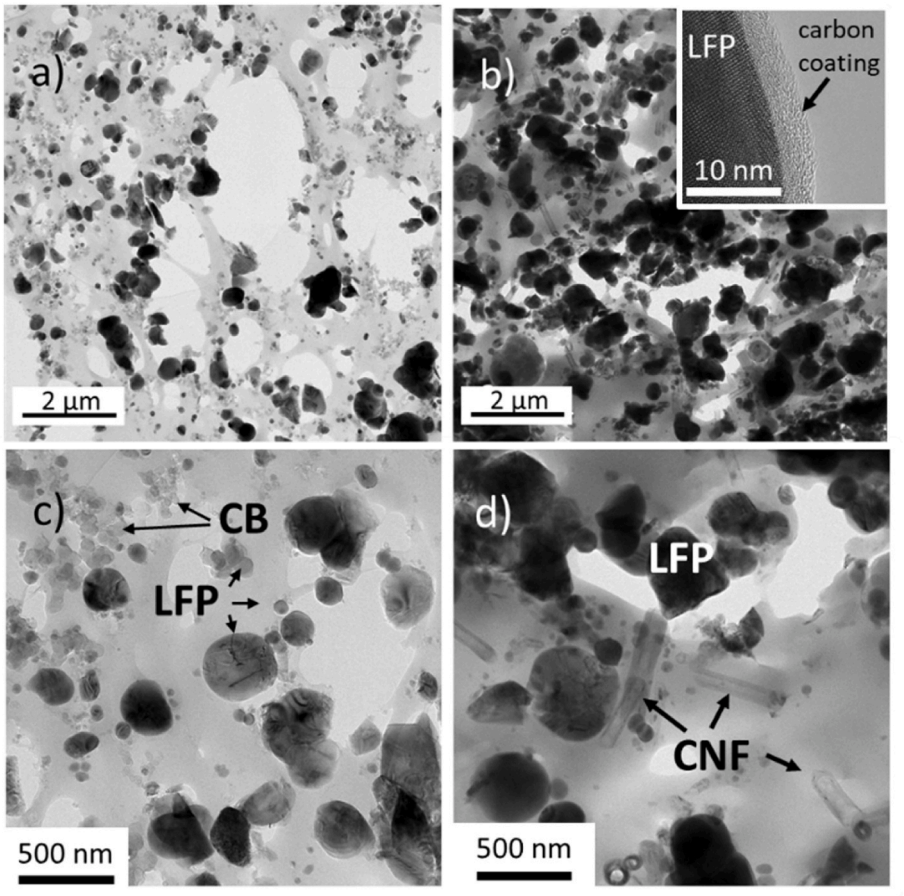

Fig. 6. Cross-sectional TEM images of the LFP positive electrode discs 3D printed from a) and c) the previously studied filament [20] composed of 33/13/49/5 wt ratio of PLA/plasticizer (PEGDME500)/LFP/carbon black and b) and d) the new filament (F2) composed of 17.8/5.9/55/5.5 wt ratio of PP/PBE/PCL/LFP/CNF. Inset b) TEM image of carbon-coated LFP material.

cross-sectional TEM images of the corresponding filaments turn out to be informative to elucidate such difference. They reveal a lower density of active material and conductive carbon in the PLA polymer matrix of the previous filaments (Fig. 6a) than in the PP/PBE-based matrix of the new filaments (Fig. 6b). Sparse in the PLA matrix in between the LFP particles, the small particles of carbon black (around 50 nm) (Fig. 6c) may not provide enough efficient electronic percolation network. On the other hand, the superior electrochemical properties of the new composites may be due to the high density of the conductive carbon-coated LFP particles (inset Fig. 6b) that can come in contact each other and the electron bridges created by the carbon fibers (Fig. 6d).

It is worth recalling that a more viscous and less conductive electrolyte consisting of EC/DEC (1/1 wt%) in 1 M $LiPF_6$ was required for cycling previous discs in order to mitigate their mechanical property loss through PLA gelation whereas the newly formulated discs with greater mechanical features can be cycled with less viscous and more conductive electrolyte; all the discs keep the same dimensions and mechanical integrity after cycling. Overall, it can be inferred that the addition of a second mechanically stable, charge-concentrating non-polar polymer, together with the use of carbon fibers to create a long-range electronic network, is a promising way of increasing the electrochemical performance of thick 3D printed discs.

3.5. Larger-scale extrusion of F2 filament

Composite of F2 formulation was extruded on a larger scale using the extruder and protocol described in the experimental section. Due to the manual and thus not optimal feeding of the extruder, the filament lacks materials in some parts and therefore was recovered in several pieces after breaking. However, as anticipated from the laboratory-scale and modelling studies, the filament was easily spoolable around the spool and its electronic conductivity value (41 ± 17 S/m) turned out to be multiplied by a factor of around 9 (Fig. 7a) compared to that obtained from lab-scale extrusion (5 ± 1 S/m). Therefore, this larger-scale extruder, owing to the multiple successive mixing/discharge screw elements, may provide a dispersive mixing, which allows the agglomerates of CNF to be more efficiently disentangled and dispersed. It should be noted that it may still be possible to improve the mixing of materials on the used lab-scale extruder by applying a counter-rotative mode rather than a co-rotative mode [33].

For sake of comparison between laboratory- and larger-scale extrusion processes, filament printing and electrochemical tests of discs were carried out following exactly the same protocols. Similar to the selective dissolution measurements performed on hereabove studied discs, the larger-scale F2 sample reveals a full accessibility of the PCL. The specific discharge capacities of both discs are found to be quite similar (Fig. 7b). Slightly higher capacities are obtained at current densities of C/10, and C/5. As shown in Fig. 7c, the potential profile of the "larger-scale" disc portrays a polarization upon charge and discharge at C/10 inferior to that of the laboratory-scale disc (70 % polarization decrease at 60 mAh. g^{-1}). This improvement in the electrochemical behaviour can be explained by the higher electronic conductivity (Fig. 7a). The limited

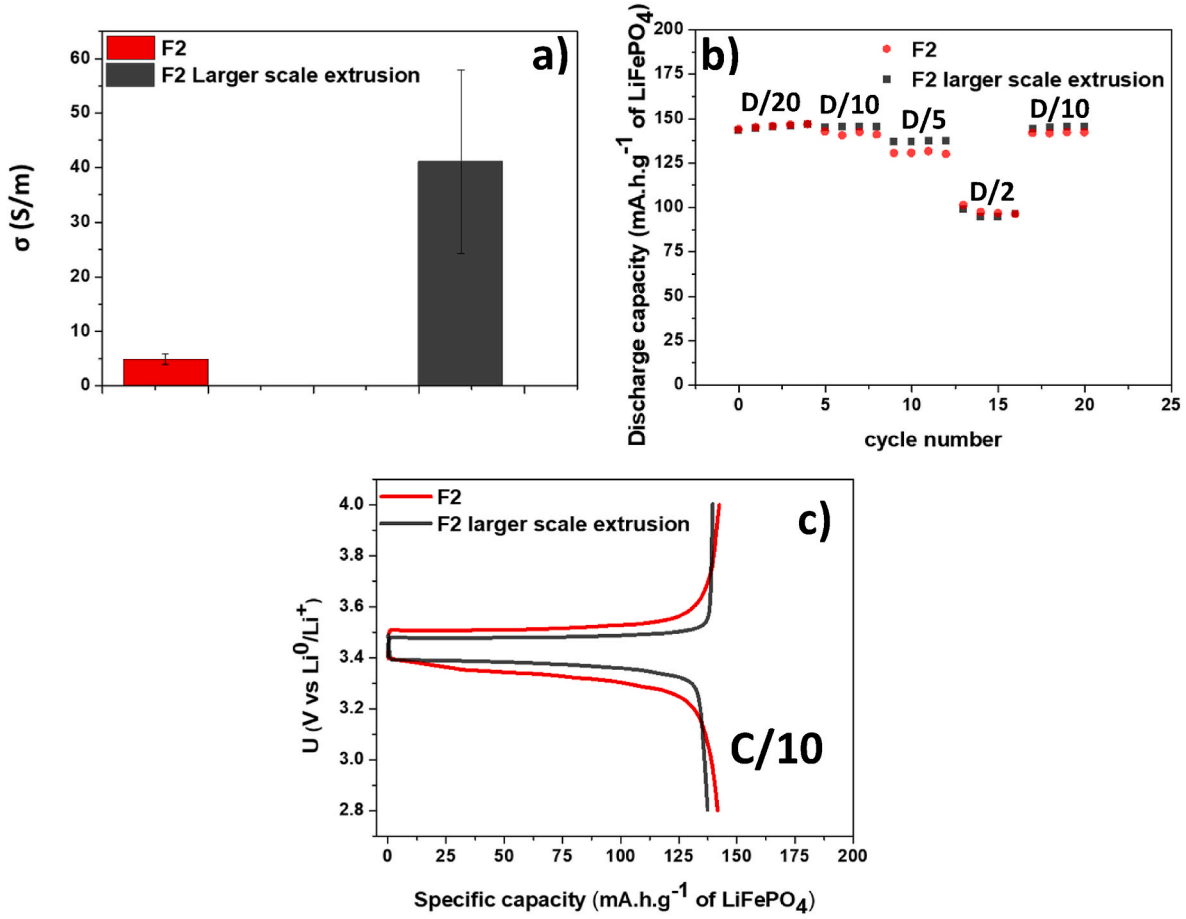

Fig. 7. a) Electronic conductivities of F2 filaments extruded at laboratory and larger scale. b) Evolution of the electrochemical discharge capacity (in mAh per gram of LFP) of half coin cells comprising 3D printed discs of F2 composition (Table 1) as the working electrode and LP37 as electrolyte. These cells have undergone the same C-rates of C/40, D/20 then C/n = D/n, n = 10, 5, 2 and 10 (D stands for C-rate upon discharge). c) Corresponding polarization curves obtained at a current rate of C/10.

capacities at C/2 (95 mAh.g^{-1}) may be due to the low ionic conductivity of the PCL-based gel electrolyte. Overall, it should be noted that, as a first printed layer, the thickness of these electrodes is necessarily very high (150-200 μm) and that higher capacities are expected at a high C-rate with thinner electrodes (around 100 μm) printed on a first collector layer.

All of these results demonstrate the importance of the extrusion process on the dispersion of electronically conductive materials and consequently on electrochemical performances. It is predictable that, owing to longer screws and adjustable mixing and discharge elements, large-scale extrusion processes should always make it possible to produce filaments from agglomerated materials with improved properties.

From a performance point of view, investigating a formulation with a higher mass fraction of active material would obviously increase the specific electrode capacity. This should be performed with the aim of maintaining a spoolable filament, while reducing the risk of frequent print issues such as nozzle clogging due to increased formulation viscosity and/or high amount of fillers. According to Beran et al. [34], irrespective of the particle size in relation to the nozzle diameter, a composition with a volumetric loading rate of more than 45 vol% should not be exceeded, thus limiting the theoretical active material mass percentage to around 67 wt%.

4. Conclusion

A significant improvement has been achieved regarding the electrochemical performance of 3D printed LFP electrode discs as compared to our pioneering study focused on a single PLA polymer-based matrix [20]. Indeed, the newly formulated composite containing a co-continuous blend of immiscible polar (PCL) and non-polar (PP) polymers allow an enhanced mechanical integrity of the disc when impregnated with liquid carbonate electrolyte. A careful examination of materials dispersion through SEM and TEM indicates that LFP active material particles are well-maintained and concentrated in the PP polymer matrix. It is assumed that the rapprochement of the carbon-coated LFP particles associated with the presence of carbon fibers to create bridges between particles offer a greater electronic network. PCL polymer domains whose role is to absorb and transport the electrolyte through the electrode are hopefully deprived from LFP particles. Interestingly, this finding was expected from the loads localization prediction study based on viscosity analysis but not from that based on the wettability coefficients. This highlights the prevailing impact of polymer rheology and extrusion parameters over the chemical affinity of loads towards polymers.

The base filament made from a 23.7/15.8/55/5.5 wt ratio of PP/PCL/LFP/CNF proved too brittle to be wound around a spool, so a solution had to be found to make it more flexible without reducing the active material content. The incorporation of plasticizers was ruled out

due to their relatively low boiling point, which causes them to partially evaporate during extrusion, printing and storage processes. The strategy of partially replacing the semi-crystalline PP polymer with a thermoplastic elastomer, an ethylene/propylene random copolymer that is also inert towards the electrolyte and known to give the blend PP/PBE greater toughness performance [29], was therefore investigated. As a large amount of PBE turned out to strongly decrease the electrochemical performances, a 25 wt% PP substitution level was considered as a good compromise in terms of printability, electrochemical performances and mechanical properties.

Last but not least, an LFP positive electrode filament of this new PBE containing formulation was successfully extruded at larger scale. The corresponding 3D printed electrode disc displays enhanced electrochemical properties as compared to the laboratory-scale extrusion process, which allows us to envisage with confidence its industrial manufacture.

CRediT authorship contribution statement

Victor Boudeville: Investigation, Methodology, Writing – original draft, Writing – review & editing. **Sylvie Grugeon:** Conceptualization, Investigation, Methodology, Writing – original draft, Writing – review & editing. **Alexis Maurel:** Conceptualization, Investigation, Methodology. **Raynald Lesieur:** Investigation. **Maroua Louati:** Investigation. **Aurélie Cayla:** Investigation, Methodology. **Sébastian Ursescu:** Investigation. **Christine Campagne:** Methodology. **Stéphane Panier:** Conceptualization, Investigation, Methodology, Writing – original draft, Writing – review & editing, Supervision. **Loic Dupont:** Conceptualization, Investigation, Supervision, Writing – review & editing, Project administration, Funding acquisition.

Declaration of competing interest

The authors declare that they have no known competing financial interests or personal relationships that could have appeared to influence the work reported in this paper.

Data availability

Data will be made available on request.

Acknowledgment

This work was performed in the frame of the IODA (ImpressiOn 3D d'Accumulateurs lithium-ion) project, funded by the ANR, research and innovation program under Grant agreement N°ANR-20-CE05-0025. Authors would like to thank Mathieu Courty, Luisa Gomes, Thibault Hery, Félix Bourseau, Erwan Leneveu, Guirec Ales either for technical support or fruitful scientific discussions and NANOVIA for its involvement in this project.

References

[1] S. Mahmud, et al., Recent advances in lithium-ion battery materials for improved electrochemical performance: a review, Results Eng 15 (2022), 100472.
[2] H. Zhang, et al., From solid-solution electrodes and the rocking-chair concept to today's batteries, Angew. Chem. Int. Ed. 59 (2) (2020) 534–538, https://doi.org/10.1002/anie.201913923.
[3] J.-M. Tarascon et, M. Armand, Issues and challenges facing rechargeable lithium batteries, Nature 414 (6861) (2001) 359–367.
[4] J.W. Long, B. Dunn, D.R. Rolison, et H.S. White, Three-dimensional battery architectures, Chem. Rev. 104 (10) (2004) 4463–4492.
[5] A. Maurel, et al., Considering lithium-ion battery 3D-printing via thermoplastic material extrusion and polymer powder bed fusion, Addit. Manuf. 37 (2021), 101651.
[6] H. Ota, et al., Application of 3D printing for smart objects with embedded electronic sensors and systems, Adv. Mater. Technol. 1 (1) (2016), 1600013.
[7] J. Lee, H.-C. Kim, J.-W. Choi, et I.H. Lee, A review on 3D printed smart devices for 4D printing, Int. J. Precis. Eng. Manuf.-Green Technol. 4 (2017) 373–383.
[8] S. Praveen, P. Santhoshkumar, Y.C. Joe, C. Senthil, et C.W. Lee, 3D-printed architecture of Li-ion batteries and its applications to smart wearable electronic devices, Appl. Mater. Today 20 (2020), 100688.
[9] S. Wu, et al., 3D printing technology for smart clothing: a topic review, Materials 15 (20) (2022) 7391.
[10] J.H. Lee, et al., 3D printed, customizable, and multifunctional smart electronic eyeglasses for wearable healthcare systems and human–machine interfaces, ACS Appl. Mater. Interfaces 12 (19) (2020) 21424–21432.
[11] R.R. Kohlmeyer, et al., Composite batteries: a simple yet universal approach to 3D printable lithium-ion battery electrodes, J. Mater. Chem. A 4 (43) (nov. 2016) 16856–16864, https://doi.org/10.1039/C6TA07610F.
[12] Y. Bao, Y. Liu, Y. Kuang, D. Fang, et T. Li, 3D-printed highly deformable electrodes for flexible lithium ion batteries, Energy Storage Mater. 33 (2020) 55–61, https://doi.org/10.1016/j.ensm.2020.07.010, déc.
[13] Y. Gu, A. Wu, H. Sohn, C. Nicoletti, Z. Iqbal, et J.F. Federici, Fabrication of rechargeable lithium ion batteries using water-based inkjet printed cathodes, J. Manuf. Process. 20 (2015) 198–205.
[14] T. Khudiyev, et al., Thermally drawn rechargeable battery fiber enables pervasive power, Mater. Today 52 (janv. 2022) 80–89, https://doi.org/10.1016/j.mattod.2021.11.020.
[15] K. Sztymela, et al., Fabrication of modern lithium ion batteries by 3D inkjet printing: opportunities and challenges, Heliyon 8 (12) (déc. 2022), e12623, https://doi.org/10.1016/j.heliyon.2022.e12623.
[16] H. Ragones, et al., Towards smart free form-factor 3D printable batteries, Sustain. Energy Fuels 2 (7) (juin 2018) 1542–1549, https://doi.org/10.1039/C8SE00122G.
[17] A. Dey, I.N. Roan Eagle, et N. Yodo, A review on filament materials for fused filament fabrication, J. Manuf. Mater. Process. 5 (3) (2021) 69.
[18] S. Singh, G. Singh, C. Prakash, et S. Ramakrishna, Current status and future directions of fused filament fabrication, J. Manuf. Process. 55 (2020) 288–306.
[19] B. Brenken, E. Barocio, A. Favaloro, V. Kunc, et R.B. Pipes, Fused filament fabrication of fiber-reinforced polymers: a review, Addit. Manuf. 21 (2018) 1–16.
[20] A. Maurel, et al., Three-dimensional printing of a LiFePO4/graphite battery cell via fused deposition modeling, Sci. Rep. 9 (1) (2019), 18031.
[21] J. Regnier, A. Cayla, C. Campagne, et É. Devaux, Melt spinning of flexible and conductive immiscible thermoplastic/elastomer monofilament for water detection, Nanomaterials 12 (1) (2021) 92.
[22] S. Chaput, C. Carrot, M. Castro, et F. Prochazka, Co-continuity interval in immiscible polymer blends by dynamic mechanical spectroscopy in the molten and solid state, Rheol. Acta 43 (2004) 417–426.
[23] X. Yan, A. Cayla, E. Devaux, et F. Salaün, Microstructure evolution of immiscible PP-PVA blends tuned by polymer ratio and silica nanoparticles, Polymers 10 (9) (2018) 1031.
[24] L. Marischal, A. Cayla, G. Lemort, C. Campagne, et É. Devaux, Selection of immiscible polymer blends filled with carbon nanotubes for heating applications, Polymers 11 (11) (2019) 1827.
[25] J. Chen, H. Hu, S. Li, et Y. He, Evolution of mechanical properties of polypropylene separator in liquid electrolytes for lithium-ion batteries, J. Appl. Polym. Sci. 135 (27) (2018), 46441.
[26] A. Cayla, C. Campagne, M. Rochery, et E. Devaux, Electrical, rheological properties and morphologies of biphasic blends filled with carbon nanotubes in one of the two phases, Synth. Met. 161 (11–12) (2011) 1034–1042.
[27] P.A. Eutionnat-Diffo, A. Cayla, Y. Chen, J. Guan, V. Nierstrasz, et C. Campagne, Development of flexible and conductive immiscible thermoplastic/elastomer monofilament for smart textiles applications using 3D printing, Polymers 12 (10) (2020) 2300.
[28] Y. Gao, J. Li, Y. Yuan, S. Huang, B. Du, Trap distribution and dielectric breakdown of isotactic polypropylene/propylene based elastomer with improved flexibility for DC cable insulation, IEEE Access 6 (2018), https://doi.org/10.1109/ACCESS.2018.2874826, 58645e58661.
[29] X. Wang, S. Hu, Y. Guo, G. Li, et R. Xu, Toughened high-flow polypropylene with polyolefin-based elastomers, Polymers 11 (12) (2019), https://doi.org/10.3390/polym11121976. Art. n° 12, déc.
[30] M. Sumita, K. Sakata, S. Asai, K. Miyasaka, et H. Nakagawa, Dispersion of fillers and the electrical conductivity of polymer blends filled with carbon black, Dispers. Fill. Electr. Conduct. Polym. Blends Fill. Carbon Black 25 (2) (1991) 265–271.
[31] S. Wu, Polymer Interface and Adhesion, first ed., Routledge, 1982 https://doi.org/10.1201/9780203742860.
[32] J. Plattier, L. Benyahia, M. Dorget, F. Niepceron, et J.-F. Tassin, Viscosity-induced filler localisation in immiscible polymer blends, Polymer 59 (2015) 260–269.
[33] R.E. Gorga et, R.E. Cohen, Toughness enhancements in poly(methyl methacrylate) by addition of oriented multiwall carbon nanotubes, J. Polym. Sci., Part B: Polym. Phys. 42 (14) (2004) 2690–2702, https://doi.org/10.1002/polb.20126.
[34] T. Beran, T. Mulholland, F. Henning, N. Rudolph, et T.A. Osswald, Nozzle clogging factors during fused filament fabrication of spherical particle filled polymers, Addit. Manuf. 23 (oct. 2018) 206–214, https://doi.org/10.1016/j.addma.2018.08.009.